Available online at www.sciencedirect.com

Acta Materialia 54 (2006) 2169–2179

www.actamat-journals.com

A dislocation density based constitutive model for crystal plasticity FEM including geometrically necessary dislocations

A. Ma, F. Roters *, D. Raabe

Max-Planck-Institut für Eisenforschung, Max-Planck-Str. 1, 40237 Düsseldorf, Germany

Received 26 April 2005; received in revised form 6 January 2006; accepted 6 January 2006
Available online 10 March 2006

Abstract

A dislocation density based constitutive model for face-centred cubic crystals is introduced and implemented into a crystal plasticity finite element framework. The approach assumes a homogeneous dislocation structure and tracks the dislocation evolution on each slip system. In addition to the statistically stored dislocations, the geometrically necessary dislocation density is introduced in order to consider strain gradients and thus render the model size sensitive. Furthermore, we develop a consistent algorithm for the updating of the geometrically necessary dislocation density. A simple shear experiment of an aluminium single crystal is used to calibrate the material parameters of the model and demonstrate its size sensitivity.

Keywords: Statistically stored dislocation density; Geometrically necessary dislocation density; Internal variables; Constitutive equation; Fcc

1. Introduction

Most polycrystalline materials reveal a nonrandom distribution of their grain orientations (crystallographic texture) which entails an overall anisotropic behavior owing to the tensorial character of most materials properties [1]. Taylor [2] was the first to formulate a model for the relationship between texture and mechanics. In his approach the local deformation for each grain is assumed to match the global one neglecting the micro-mechanical interaction among grains (full constraints model). Based on this stiff model, various variants of relaxed constraints and self-consistent homogenization models were introduced which allow some of the strain constraints among the grains to be dropped [3–7].

Most polycrystal mechanics models use rather simple constitutive formulations where the flow and hardening rules are often described as powers laws. While for homogeneous materials viscoplastic formulations are useful they reveal disadvantages when the simulation scale becomes so small that size effects matter [8–10]. Such size effects lead to nonuniform plastic deformation entailing strain and orientation gradients. Therefore, a certain amount of extra dislocations must be introduced for preserving lattice continuity. This means that local constitutive models should be extended to nonlocal ones, which can consider the interplay between texture and dislocation evolution on the basis of divergent behavior of neighboring material points. Since local crystalline orientation gradients are necessarily associated with the storage of geometrically necessary dislocations (GNDs), it is an obvious requirement that a nonlocal constitutive model should be built on dislocation densities rather than on empirical hardening functions.

In this study a local constitutive model based on dislocation densities [11] will be extended to a nonlocal one in the following way: First the cell structure composed of cell blocks (CBs) and dense dislocation walls (DDWs) as used in the earlier model [11] is reduced in this approach to a homogeneous structure. Second, in addition to the

---

* Corresponding author. Tel.: +49 211 6792 393; fax: +49 211 6792 333.
E-mail address: roters@mpie.de (F. Roters).

1359-6454/$30.00 © 2006 Acta Materialia Inc. Published by Elsevier Ltd. All rights reserved.
doi:10.1016/j.actamat.2006.01.005

statistically stored dislocations (SSDs), GNDs are introduced to accommodate local orientation gradients. The storage of SSDs results mainly from random trapping processes of mobile dislocations. Such arrangements are characterised by a vanishing net Burgers vector. In contrast, the storage of GNDs leads to a polarized dislocation density resulting from the curvature of the crystal lattice under incompatible plastic strains. Another important difference between the two types of stored dislocations is that the GNDs assume a tensorial form. Third, the evolution of the dislocations is tracked separately for each slip system which is an advantage inherent to the crystal plasticity approach. Fourth, the SSDs on each slip system are divided into mobile and immobile dislocations. While the former ones accommodate the external plastic deformation the latter ones are responsible for hardening. The resistance against the motion of a mobile dislocation on the slip system α results from passing stresses caused by parallel dislocations ($\rho_{\mathrm{P}}^{\alpha}$) and cutting stresses resulting from forest dislocations ($\rho_{\mathrm{F}}^{\alpha}$). Therefore, a projection procedure is used for all GNDs and immobile SSDs in order to calculate parallel and forest dislocations for every slip system. Fifth, a scaling relation between the mobile dislocations and the forest and parallel ones is adopted which is based on maximizing the plastic dissipation for a fixed external resolved shear stress [11]. Other model features are similar to earlier formulations, i.e. the Orowan expression serves as the kinetic equation and the evolution laws for the immobile SSDs are formulated as rate equations based on distinct dislocation processes such as lock formation or annihilation via climb. Since the flow and hardening rules of the model contain all relevant basic formulations of thermally activated processes, the rate and temperature dependencies are included in a generic fashion [11].

The implementation of a nonlocal dislocation density based constitutive model into a crystal plasticity finite element (FE) framework raises a number of fundamental issues. In order to solve the evolution law for the GND density the gradient of the shear rates of every slip system must be calculated for each Gauss point. In order to meet these requirements some authors [12,13] used the divergence theorem for the transformation of the shear rates and the plastic deformation gradient into dislocation densities. In this framework GNDs and SSDs have been treated as additional degrees of freedom for every node and a Newton–Raphson iterative procedure is introduced to achieve the solution for the SSD and GND densities. Such an algorithm relies on an additional dislocation density flux boundary condition, which, however, is difficult to formulate for complicated forming processes. Another drawback of this algorithm is the complex coding required prior to its use. Therefore, in Section 4 of this paper we introduce another integration algorithm to derive the solution for any nonlocal constitutive model based on the general material subroutines of commercial FEM software such as MSC.Marc and Abaqus.

2. The constitutive formulations

2.1. Kinematics

The deformation gradient, $\mathbf{F} = \partial\mathbf{x}/\partial\mathbf{X}$, is decomposed according to [14]

$$\mathbf{F} = \mathbf{F}_{\mathrm{e}}\mathbf{F}_{\mathrm{p}}, \tag{1}$$

where $\mathbf{F}_{\mathrm{e}}$ is the elastic part comprising the stretch, $\mathbf{U}_{\mathrm{e}}$, and the lattice rotation, $\mathbf{R}_{\mathrm{e}}$, and $\mathbf{F}_{\mathrm{p}}$ corresponds to the plastic deformation caused by dislocation slip. Stretch and rotation are obtained from the polar decomposition $\mathbf{F}_{\mathrm{e}} = \mathbf{R}_{\mathrm{e}}\mathbf{U}_{\mathrm{e}}$. The elastic and the plastic deformation gradients are

$$\dot{\mathbf{F}}_{\mathrm{e}} = \mathbf{L}\mathbf{F}_{\mathrm{e}} - \mathbf{F}_{\mathrm{e}}\mathbf{L}_{\mathrm{p}}, \quad \dot{\mathbf{F}}_{\mathrm{p}} = \mathbf{L}_{\mathrm{p}}\mathbf{F}_{\mathrm{p}}, \tag{2}$$

where $\mathbf{L} = \dot{\mathbf{F}}\mathbf{F}^{-1}$ and $\mathbf{L}_{\mathrm{p}} = \dot{\mathbf{F}}_{\mathrm{p}}\mathbf{F}_{\mathrm{p}}^{-1}$ are the total and the plastic velocity gradients defined in the current and the unloaded configuration, respectively.

2.2. The elastic law

For a single crystal the mapping $\mathbf{F}_{\mathrm{p}}$ will not change the lattice orientation, i.e. we can use a constant stiffness tensor $\widetilde{\mathscr{K}}_0$ for the stress calculations when the elastic law is defined in the unloaded configuration. By defining the second Piola–Kirchhoff stress tensor $\widetilde{\mathbf{S}}$ in the unloaded configuration and its work conjugated elastic Green strain tensor $\widetilde{\mathbf{E}}$, the elastic law is derived as

$$\widetilde{\mathbf{S}} = \widetilde{\mathscr{K}}_0\widetilde{\mathbf{E}} \quad \text{with} \quad \widetilde{\mathbf{E}} = \frac{1}{2}(\widetilde{\mathbf{C}} - \mathbf{I}), \ \widetilde{\mathbf{C}} = \mathbf{F}_{\mathrm{e}}^{\mathrm{T}}\mathbf{F}_{\mathrm{e}}, \tag{3}$$

where $\mathbf{I}$ is the unity tensor and $\widetilde{\mathbf{C}}$ is the elastic right Cauchy–Green tensor. When the variational form is derived in the reference or current configuration, the second Piola–Kirchhoff stress $\mathbf{S}$ or the Cauchy stress $\boldsymbol{\sigma}$ amounts to

$$\mathbf{S} = \mathbf{F}_{\mathrm{p}}^{-1}\widetilde{\mathbf{S}}\mathbf{F}_{\mathrm{p}}^{-\mathrm{T}}, \quad \boldsymbol{\sigma} = \frac{1}{J}\mathbf{F}_{\mathrm{e}}\widetilde{\mathbf{S}}\mathbf{F}_{\mathrm{e}}^{\mathrm{T}}, \tag{4}$$

where $J = \det(\mathbf{F}) = \det(\mathbf{F}_{\mathrm{e}})$, which means isochoric plastic deformation is assumed, i.e. the volume change is always purely elastic.

Owing to the different grain orientations in a polycrystal in a global coordinate system, different stiffness tensors, slip plane normals and slip directions must be specified for every crystal. In order to use only one set of data a virtual deformation step is introduced before the calculation in the form: $\mathbf{F}_{\mathrm{p}0}$ is set as the initial value for $\mathbf{F}_{\mathrm{p}}$. By choosing $\mathbf{F}_{\mathrm{e}0}$ to satisfy

$$\mathbf{F}_{\mathrm{e}0}\mathbf{F}_{\mathrm{p}0} = \mathbf{I}, \quad \mathbf{F}_{\mathrm{e}0}, \mathbf{F}_{\mathrm{p}0} \in \mathrm{Orth}. \tag{5}$$

the starting value for $\mathbf{F}$ amounts to $\mathbf{I}$ as desired. As shown for two examples in Fig. 1, this procedure allows us to use the cube orientation as the starting reference configuration for all crystals.

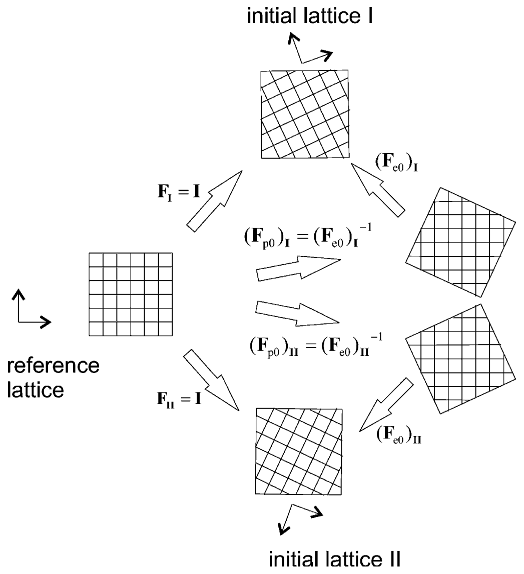

Fig. 1. Virtual deformation step to define the initial value for the plastic portion of the deformation gradient $\mathbf{F}_{\mathrm{p}}$ for every crystal of a polycrystalline aggregate. $\mathbf{F}_{\mathrm{p0}}$ and $\mathbf{F}_{\mathrm{e0}}$ are the plastic and elastic parts, respectively, of the deformation gradient $\mathbf{F} = \mathbf{I}$ of the virtual deformation step. The indices I and II refer to two different crystal orientations.

2.3. The flow rule

2.3.1. The constitutive assumption

The mobile dislocations in face-centred cubic (fcc) crystals slip on the planes with the lowest Peierls potential $\{1\,1\,1\}$ along the closest packed directions $\langle 1\,1\,0\rangle$. These slip systems can be described by the Schmid tensor $\widetilde{\mathbf{M}}^{\alpha} = \widetilde{\mathbf{d}}^{\alpha} \otimes \widetilde{\mathbf{n}}^{\alpha}$ where $\widetilde{\mathbf{d}}^{\alpha} = \mathbf{b}/b$ expresses the slip direction, which is parallel to the Burgers vector $\mathbf{b}$ but normalized, and $\widetilde{\mathbf{n}}^{\alpha}$ the slip plane normal with respect to the undistorted configuration. α is used as the slip system index. The connection between the continuum variables and the process of dislocation slip is given by

$$\mathbf{L}_{\mathrm{p}} = \sum_{\alpha=1}^{N} \dot{\gamma}^{\alpha} \widetilde{\mathbf{M}}^{\alpha}, \quad \dot{\mathbf{F}}_{\mathrm{p}} = \sum_{\alpha=1}^{N} \dot{\gamma}^{\alpha} \widetilde{\mathbf{M}}^{\alpha} \mathbf{F}_{\mathrm{p}}, \tag{6}$$

where $\dot{\gamma}^{\alpha}$ is the slip rate on the slip system α. The sum is taken over all active slip systems, i.e. in the fcc case $N = 12$ at room temperature.

2.3.2. The Orowan equation as kinetic equation of state

Commonly used expressions for the relation of the shear rate $\dot{\gamma}^{\alpha}$ and the shear stress τ^{α} are phenomenological visco-plastic rules in the form of a power law [15] or more physically-based ones [16,17] which account for rate effects and temperature. In this paper, we use the Orowan equation to calculate the plastic shear rate $\dot{\gamma}^{\alpha}$ of each slip system α as a function of the mobile dislocation density $\rho_{\mathrm{M}}^{\alpha}$ on that slip system

$$\dot{\gamma}^{\alpha} = \rho_{\mathrm{M}}^{\alpha}\, b\, v^{\alpha}, \tag{7}$$

where the average velocity of the mobile dislocations, v^{α}, depends on the resolved shear stress, τ^{α}, on the dislocation densities, $\rho_{\mathrm{M}}^{\alpha}$, $\rho_{\mathrm{F}}^{\alpha}$ and $\rho_{\mathrm{P}}^{\alpha}$, and on the temperature, θ, i.e.

$$v^{\alpha} = v^{\alpha}(\tau^{\alpha}, \rho_{\mathrm{M}}^{\alpha}, \rho_{\mathrm{F}}^{\alpha}, \rho_{\mathrm{P}}^{\alpha}, \theta). \tag{8}$$

The resolved shear stress τ^{α} is the projection of the stress measure onto the slip system α. In the case of infinitesimally small elastic stretches, τ^{α} can be approximated as [4]

$$\tau^{\alpha} = \tilde{\mathbf{S}}\tilde{\mathbf{C}} \cdot \widetilde{\mathbf{M}}^{\alpha} \cong \tilde{\mathbf{S}} \cdot \widetilde{\mathbf{M}}^{\alpha}. \tag{9}$$

The mobile dislocations, $\rho_{\mathrm{M}}^{\alpha}$, slide along slip system α to accommodate a part of the external plastic deformation. In order to do so they must overcome the stress field of the parallel dislocations, $\rho_{\mathrm{P}}^{\alpha}$, which cause the passing stress. Also they must cut the forest dislocations, $\rho_{\mathrm{F}}^{\alpha}$, with the aid of thermal activation, see Fig. 2. We define the parallel dislocation density, $\rho_{\mathrm{P}}^{\alpha}$, and the forest dislocation density, $\rho_{\mathrm{F}}^{\alpha}$, for slip system α as: $\rho_{\mathrm{P}}^{\alpha}$ all dislocations parallel to the slip plane, and $\rho_{\mathrm{F}}^{\alpha}$ the dislocations perpendicular to the slip plane. Both $\rho_{\mathrm{SSD}}^{\alpha}$ and $\rho_{\mathrm{GND}}^{\alpha}$ contribute to $\rho_{\mathrm{F}}^{\alpha}$ and $\rho_{\mathrm{P}}^{\alpha}$.

The mobile dislocation density belongs to the SSDs and it should, therefore, also be projected into the slip plane. However, the density of the mobile dislocations was shown to be smaller by at least one order of magnitude compared to the density of the immobile ones [11], which means that we can neglect them and consider the immobile density, ρ_{SSD}, as the total SSD density. We introduce the interaction strength, $\chi^{\alpha\beta}$, between different slip systems, which includes the self interaction strength, coplanar interaction strength, cross slip strength, glissile junction strength, Hirth lock strength, and Lomer–Cottrell lock strength. In this formulation we only consider edge dislocations owing to their limited mobility, and use a single set of interaction strengths for both SSDs and GNDs.

In order to calculate $\rho_{\mathrm{F}}^{\alpha}$ and $\rho_{\mathrm{P}}^{\alpha}$, we must first determine the tangent vectors for SSDs and GNDs. From the fact that all the immobile SSDs are created as reaction products of mobile dislocations, we can define their tangent vector as the cross product of the slip plane normal and the slip direction, $\tilde{\mathbf{t}}^{\beta} = \tilde{\mathbf{n}}^{\beta} \times \tilde{\mathbf{d}}^{\beta}$, as only edge dislocations are considered. However, this is not the case for the GNDs as this class of dislocations only preserves the continuity of the

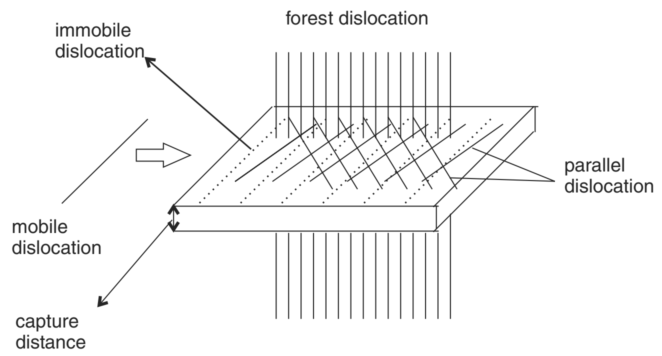

Fig. 2. Schematic drawing of the slip mechanism for the fcc crystal structure.

lattice when orientation gradients occur, i.e. it is not bound to any particular slip system. As a result the tangent vector of the GNDs may not be parallel to $\tilde{\mathbf{t}}^\beta$. More generally we assume that $\mathbf{t}^\beta_{\mathrm{GND}}$ is a function of the local orientation gradient. One way to handle this problem is to divide $\rho^\beta_{\mathrm{GND}}$ into three fractions with respect to $\tilde{\mathbf{d}}^\beta$, $\tilde{\mathbf{t}}^\beta$ and $\tilde{\mathbf{n}}^\beta$, and to define three kinds of effective GND densities $\rho^\beta_{\mathrm{GNDs}}$, $\rho^\beta_{\mathrm{GNDet}}$ and $\rho^\beta_{\mathrm{GNDen}}$ for the projection procedure, as shown in detail in Section 3.2 and Fig. 3.

By using this approach, the projection for the forest dislocation density, ρ^α_{F}, and for the parallel dislocation density, ρ^α_{P}, introduced in Ref. [11] can be extended as follows:

$$\rho^\alpha_{\mathrm{F}} = \sum_{\beta=1}^{N} \chi^{\alpha\beta}[\rho^\beta_{\mathrm{SSD}}|\cos(\tilde{\mathbf{n}}^\alpha, \tilde{\mathbf{t}}^\beta)| + |\rho^\beta_{\mathrm{GNDs}}\cos(\tilde{\mathbf{n}}^\alpha, \tilde{\mathbf{d}}^\beta)| + |\rho^\beta_{\mathrm{GNDet}}\cos(\tilde{\mathbf{n}}^\alpha, \tilde{\mathbf{t}}^\beta)| + |\rho^\beta_{\mathrm{GNDen}}\cos(\tilde{\mathbf{n}}^\alpha, \tilde{\mathbf{n}}^\beta)|], \tag{10}$$

$$\rho^\alpha_{\mathrm{P}} = \sum_{\beta=1}^{N} \chi^{\alpha\beta}[\rho^\beta_{\mathrm{SSD}}|\sin(\tilde{\mathbf{n}}^\alpha, \tilde{\mathbf{t}}^\beta)| + |\rho^\beta_{\mathrm{GNDs}}\sin(\tilde{\mathbf{n}}^\alpha, \tilde{\mathbf{d}}^\beta)| + |\rho^\beta_{\mathrm{GNDet}}\sin(\tilde{\mathbf{n}}^\alpha, \tilde{\mathbf{t}}^\beta)| + |\rho^\beta_{\mathrm{GNDen}}\sin(\tilde{\mathbf{n}}^\alpha, \tilde{\mathbf{n}}^\beta)|], \tag{11}$$

where the absolute value of the GND density is used, i.e. the sign of its net Burgers vector is ignored. As a direct result no kinematic hardening can be predicted, which is, however, less relevant in the case of unidirectional loading.

2.3.3. Relation between mobile and immobile dislocation densities

When integrating the velocity equation (8) into the Orowan equation (7), it becomes apparent that the shear rate $\dot{\gamma}^\alpha$ is a nonlinear function of ρ^α_{M}. From [11,18] we know that by applying the principle of maximum plastic dissipation for the external resolved shear stress during the plastic deformation

$$\left(\frac{\partial \dot{\gamma}^\alpha}{\partial \rho^\alpha_{\mathrm{M}}}\right)_{\tau^\alpha, \rho^\alpha_{\mathrm{F}}, \rho^\alpha_{\mathrm{P}}, \theta} = 0 \tag{12}$$

a scaling relation can be derived for the homogeneous dislocation structure which amounts to

$$\rho^\alpha_{\mathrm{M}} \approx B\theta\sqrt{\rho^\alpha_{\mathrm{P}}\rho^\alpha_{\mathrm{F}}} \quad \text{with } B = \frac{2k_{\mathrm{B}}}{c_1c_2c_3Gb^3}, \tag{13}$$

where c_1, c_2, c_3 are constants, G is the shear modulus, and k_{B} the Boltzmann constant. See details in Ref. [11].

This means that the mobile dislocation density is proportional to the geometric mean of the parallel and the forest dislocation densities. Moreover, the fraction of mobile dislocations increases linearly with the temperature, which is reasonable as dislocation glide is a thermally activated process. Eq. (13) forms an intrinsic constraint equation for the dislocation structure. It implies that the dislocation structure with three sets of independent internal variables $(\rho^\alpha_{\mathrm{M}}, \rho^\alpha_{\mathrm{SSD}}, \rho^\alpha_{\mathrm{GND}}, \alpha = 1, N)$ has been reduced to one with only two sets of independent internal variables $(\rho^\alpha_{\mathrm{SSD}}, \rho^\alpha_{\mathrm{GND}}, \alpha = 1, N)$.

2.3.4. The flow rule based on dislocation mechanisms

Conventional flow rules use a reference shear rate and a rate sensitivity exponent which are typically constant. In this paper a new flow rule is derived based on dislocation slip. It includes a reference shear rate which is a function of the dislocation density and the temperature,

$$\dot{\gamma}^\alpha = \begin{cases} \dot{\gamma}^\alpha_0 \exp\left[-\frac{Q_{\mathrm{slip}}}{k_{\mathrm{B}}\theta}\left(1 - \frac{|\tau^\alpha| - \tau^\alpha_{\mathrm{pass}}}{\tau^\alpha_{\mathrm{cut}}}\right)\right] \mathrm{sign}(\tau^\alpha), & |\tau^\alpha| > \tau^\alpha_{\mathrm{pass}}, \\ 0, & |\tau^\alpha| \leqslant \tau^\alpha_{\mathrm{pass}} \end{cases} \tag{14}$$

with the pre-exponential variable $\dot{\gamma}^\alpha_0$, which is the upper limit of the shear rate for the case where the Boltzmann factor is equal to 1 in Eq. (14)

$$\dot{\gamma}^\alpha_0 = \frac{k_{\mathrm{B}}\theta}{c_1c_3Gb^2}\sqrt{\rho^\alpha_{\mathrm{P}}} \tag{15}$$

and the passing stress, $\tau^\alpha_{\mathrm{pass}}$, caused by the parallel dislocations

$$\tau^\alpha_{\mathrm{pass}} = c_1Gb\sqrt{\rho^\alpha_{\mathrm{P}}} \tag{16}$$

and the cutting stress, $\tau^\alpha_{\mathrm{cut}}$, at 0 K caused by the forest dislocations

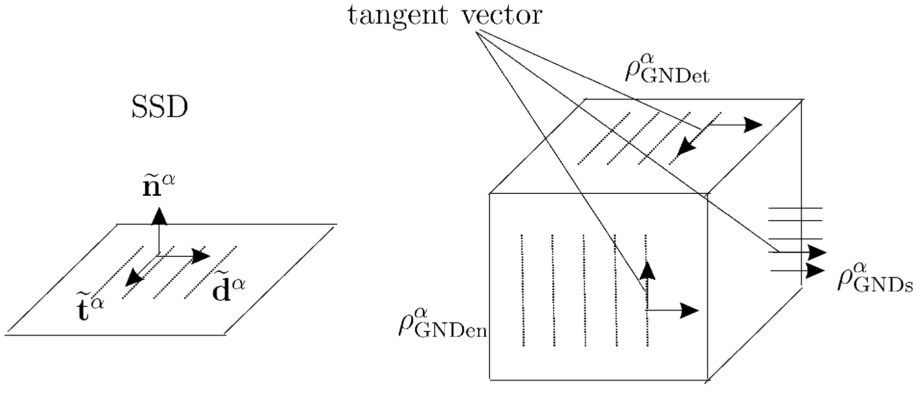

Fig. 3. Schematic drawing of the geometric configurations for the SSDs and the GNDs. The GND density is split into three fractions. Two fractions with edge character ($\rho^\alpha_{\mathrm{GNDet}}, \rho^\alpha_{\mathrm{GNDen}}$) parallel to $\tilde{\mathbf{t}}^\alpha$ and $\tilde{\mathbf{n}}^\alpha$, respectively, and one with screw character ($\rho^\alpha_{\mathrm{GNDs}}$) parallel to $\tilde{\mathbf{d}}^\alpha$.

$$\tau^\alpha_{\mathrm{cut}} = \frac{Q_{\mathrm{slip}}}{c_2 c_3 b^2}\sqrt{\rho^\alpha_{\mathrm{F}}}, \tag{17}$$

where Q_{slip} is the effective activation energy for dislocation slip.

3. Evolution of the densities of the statistically stored and geometrically necessary dislocations

3.1. The evolution of the statistically stored dislocation density

There are four processes contributing to the evolution of the immobile SSDs. The lock forming mechanism between mobile dislocations and forest dislocations, and the dipole forming mechanism between mobile dislocations with anti-parallel Burgers vector determine the multiplication terms, while the athermal annihilation of two parallel dislocations with anti-parallel Burgers vector within a critical distance and the thermal annihilation by climb of edge dislocations determine the annihilation terms. The complete rate equation for the immobile SSD combines these four processes

$$\begin{aligned}\dot{\rho}^\alpha_{\mathrm{SSD}} = {} & c_4\sqrt{\rho^\alpha_{\mathrm{F}}}\,\dot{\gamma}^\alpha + c_6 d^\alpha_{\mathrm{dipole}}\rho^\alpha_{\mathrm{M}}\dot{\gamma}^\alpha - c_5\rho^\alpha_{\mathrm{SSD}}\dot{\gamma}^\alpha \\ & - c_7 \exp\left(-\frac{Q_{\mathrm{bulk}}}{k_{\mathrm{B}}\theta}\right)\frac{|\tau^\alpha|}{k_{\mathrm{B}}\theta}\left(\rho^\alpha_{\mathrm{SSD}}\right)^2\dot{\gamma}^{c_8}\end{aligned} \tag{18}$$

with c_4–c_8 being constants, d_{dipole} the critical distance for dipole formation, and Q_{bulk} the activation energy for self diffusion. Details are given in Ref. [11].

3.2. The evolution of the geometrically necessary dislocation density

In the presence of orientation gradients GNDs must be introduced to preserve the lattice continuity. A relation between a possible GND measure and the plastic deformation gradient has been proposed by Nye [19]. This approach has been later extended to a more physically motivated continuum approach to generally account for strain gradient effects by Dai and Parks [20,21]. Following these pioneering approaches we use as a dislocation density tensor for a selected volume portion and Burgers circuit

$$\mathbf{\Lambda} = -\frac{1}{b}\left(\mathbf{\nabla}_X \times \mathbf{F}^{\mathrm{T}}_{\mathrm{p}}\right)^{\mathrm{T}}, \tag{19}$$

where nabla, $\mathbf{\nabla}_X$, is defined as the derivative with respect to the reference coordinates, i.e. $\mathbf{\nabla}_X = \partial/\partial\mathbf{X}$. If the gradient is calculated in the current configuration we use the definition $\mathbf{\nabla}_x = \partial/\partial\mathbf{x}$. Using Eq. (19) the resulting Burgers vector for a circuit with an arbitrary orientation can be calculated. In general this tensor is nonsymmetric and it can be mapped to nine independent slip systems in a unique fashion. For the fcc crystal structure with its 12 slip systems for the SSDs only five systems are independent according to the von Mises–Taylor constraint. This implies that it is impossible to calculate the exact amount of GNDs for every slip system in a unique way as for the SSDs. As a result the tangent vector, $\mathbf{t}^\alpha_{\mathrm{GND}}$, cannot be kept constant, but it should evolve as a function of strain as already shown for the scalar variable $\rho^\alpha_{\mathrm{GND}}$.

When using the material time derivative of Eq. (19) and the result from Eq. (6) we obtain

$$\dot{\mathbf{\Lambda}} = \sum_{\alpha=1}^{N} -\frac{1}{b}\tilde{\mathbf{d}}^\alpha \otimes \left[\mathbf{\nabla}_X \times \left(\dot{\gamma}^\alpha \mathbf{F}^{\mathrm{T}}_{\mathrm{p}}\right)\tilde{\mathbf{n}}^\alpha\right] = \sum_{\alpha=1}^{N}\dot{\mathbf{\Lambda}}^\alpha. \tag{20}$$

Eq. (20) defines a normal vector for the GNDs of slip system α. In this context we assume again that the tangent vector is parallel to the normal vector of the slip system for the case where the dislocation density is defined as the piercing density through the slip plane

$$\mathbf{n}^\alpha_{\mathrm{GND}} = \mathbf{t}^\alpha_{\mathrm{GND}} = \frac{1}{\dot{\rho}^\alpha_{\mathrm{GND}}}\left[\frac{1}{b}\mathbf{\nabla}_X \times \left(\dot{\gamma}^\alpha \mathbf{F}^{\mathrm{T}}_{\mathrm{p}}\right)\tilde{\mathbf{n}}^\alpha\right] \tag{21}$$

with

$$\dot{\rho}^\alpha_{\mathrm{GND}} = \frac{1}{b}\left\|\mathbf{\nabla}_X \times \left(\dot{\gamma}^\alpha \mathbf{F}^{\mathrm{T}}_{\mathrm{p}}\right)\tilde{\mathbf{n}}^\alpha\right\|. \tag{22}$$

Up to now it has not been pertinent to project $\rho^\alpha_{\mathrm{GND}}$ into forest and parallel dislocations because the tangent vector of the GNDs is not constant. Although in this paper SSDs are assumed to be edge dislocations only, for the GND analysis we have to account for edge and screw dislocations. $\dot{\mathbf{\Lambda}}^\alpha$ can then be decomposed into three groups of dislocations, namely, one group of screw dislocations with their tangent vector parallel to the slip direction $\tilde{\mathbf{d}}^\alpha$, and two groups of edge dislocations with their respective tangent vectors parallel to $\tilde{\mathbf{n}}^\alpha$ and $\tilde{\mathbf{t}}^\alpha$, i.e.

$$\dot{\mathbf{\Lambda}}^\alpha = -\dot{\rho}^\alpha_{\mathrm{GNDs}}\tilde{\mathbf{d}}^\alpha \otimes \tilde{\mathbf{d}}^\alpha - \dot{\rho}^\alpha_{\mathrm{GNDet}}\tilde{\mathbf{d}}^\alpha \otimes \tilde{\mathbf{t}}^\alpha - \dot{\rho}^\alpha_{\mathrm{GNDen}}\tilde{\mathbf{d}}^\alpha \otimes \tilde{\mathbf{n}}^\alpha \tag{23}$$

and the scalar dislocation densities to

$$\dot{\rho}^\alpha_{\mathrm{GNDs}} = \dot{\mathbf{\Lambda}}^\alpha \cdot \left(\tilde{\mathbf{d}}^\alpha \otimes \tilde{\mathbf{d}}^\alpha\right), \tag{24}$$

$$\dot{\rho}^\alpha_{\mathrm{GNDet}} = \dot{\mathbf{\Lambda}}^\alpha \cdot \left(\tilde{\mathbf{d}}^\alpha \otimes \tilde{\mathbf{t}}^\alpha\right), \tag{25}$$

$$\dot{\rho}^\alpha_{\mathrm{GNDen}} = \dot{\mathbf{\Lambda}}^\alpha \cdot \left(\tilde{\mathbf{d}}^\alpha \otimes \tilde{\mathbf{n}}^\alpha\right) \tag{26}$$

which satisfies

$$\left(\dot{\rho}^\alpha_{\mathrm{GND}}\right)^2 = \left(\dot{\rho}^\alpha_{\mathrm{GNDs}}\right)^2 + \left(\dot{\rho}^\alpha_{\mathrm{GNDet}}\right)^2 + \left(\dot{\rho}^\alpha_{\mathrm{GNDen}}\right)^2. \tag{27}$$

4. Consistent time integration scheme for the nonlocal model

4.1. The global control equations

Starting from the standard displacement based FE analysis in conjunction with the total Lagrangian approach, the equilibrium can be expressed using the principle of virtual work

$$\int_{V_0} \mathbf{S} \cdot \delta\mathbf{E}\,\mathrm{d}V_0 = \int_{V_0} \mathbf{t}_{v0} \cdot \delta\mathbf{u}\,\mathrm{d}V_0 + \int_{S_0} \mathbf{t}_{s0} \cdot \delta\mathbf{u}\,\mathrm{d}S_0, \tag{28}$$

where $\mathbf{t}_{v0}$ is the body force, $\mathbf{t}_{s0}$ is the surface traction, and $\delta\mathbf{u}$ is an arbitrary virtual displacement field. $\mathbf{E}$ is the total Green–Lagrangian strain

$$\mathbf{E} = \frac{1}{2}(\mathbf{F}^{\mathrm{T}}\mathbf{F} - \mathbf{I}) \tag{29}$$

and the virtual strain $\delta\mathbf{E}$ caused by the virtual displacement field $\delta\mathbf{u}$ is

$$\delta\mathbf{E} = \frac{1}{2}\left[\left(\frac{\partial\delta\mathbf{u}}{\partial\mathbf{X}}\right)^{\mathrm{T}}\frac{\partial\mathbf{x}}{\partial\mathbf{X}} + \left(\frac{\partial\mathbf{x}}{\partial\mathbf{X}}\right)^{\mathrm{T}}\frac{\partial\delta\mathbf{u}}{\partial\mathbf{X}}\right]. \tag{30}$$

For the isoparametric element the virtual field, $\delta\mathbf{u}$, can be interpolated as a function of the nodal values, $\delta\hat{\mathbf{u}}_I$, via the shape function values N_I

$$\delta\mathbf{u} = \sum_I N_I \delta\hat{\mathbf{u}}_I \tag{31}$$

and the virtual strain changes to

$$\delta\mathbf{E} = \frac{1}{2}\sum_I [(\delta\hat{\mathbf{u}}_I \otimes \mathbf{\nabla}_X N_I)^{\mathrm{T}}\mathbf{F} + \mathbf{F}^{\mathrm{T}}(\delta\hat{\mathbf{u}}_I \otimes \mathbf{\nabla}_X N_I)]. \tag{32}$$

An equivalent expression can be derived for the strain increment, $\delta\epsilon$, defined in the current configuration

$$\begin{aligned}\delta\epsilon &= \mathbf{F}^{-\mathrm{T}}\delta\mathbf{E}\mathbf{F}^{-1}\\ &= \frac{1}{2}\sum_I [\mathbf{F}^{-\mathrm{T}}(\delta\hat{\mathbf{u}}_I \otimes \mathbf{\nabla}_X N_I)^{\mathrm{T}} + (\delta\hat{\mathbf{u}}_I \otimes \mathbf{\nabla}_X N_I)\mathbf{F}^{-1}]\\ &= \frac{1}{2}\sum_I [(\delta\hat{\mathbf{u}}_I \otimes \mathbf{\nabla}_x N_I) + (\delta\hat{\mathbf{u}}_I \otimes \mathbf{\nabla}_x N_I)^{\mathrm{T}}],\end{aligned} \tag{33}$$

where $\mathbf{\nabla}_x = \mathbf{\nabla}_X \mathbf{F}^{-1}$ is defined in the current configuration.

When inserting this result into the virtual work equation (28), and considering the symmetry of the stress tensor and the arbitrarily chosen virtual displacements, $\delta\hat{\mathbf{u}}_I$, Eq. (28) becomes equivalent to the equation for the residual force $\mathbf{H}(\hat{\mathbf{u}})$ in the current configuration

$$\mathbf{H}(\hat{\mathbf{u}}) = \int_V (\mathbf{\nabla}_x N_I)^{\mathrm{T}}\boldsymbol{\sigma}\,\mathrm{d}V - \int_V N_I \mathbf{t}_{\mathrm{v}}\,\mathrm{d}V - \int_S N_I \mathbf{t}_{\mathrm{s}}\,\mathrm{d}S = 0, \tag{34}$$

where $\mathbf{t}_{\mathrm{v}}$ is the body force and $\mathbf{t}_{\mathrm{s}}$ is the surface traction in the current configuration. For solving Eq. (34) the Newton–Raphson procedure is used to update the displacement $\hat{\mathbf{u}}$ step by step until the desired precision is reached

$$\hat{\mathbf{u}}^{n+1} = \hat{\mathbf{u}}^{n} - \left(\frac{\partial\mathbf{H}}{\partial\hat{\mathbf{u}}}\right)^{-1}_{n}\mathbf{H}_n. \tag{35}$$

$$\frac{\partial\mathbf{H}}{\partial\hat{\mathbf{u}}} = \int_V (\mathbf{\nabla}_x N_I)^{\mathrm{T}}\mathscr{K}(\mathbf{\nabla}_x N_I)\,\mathrm{d}V + \int_V (\mathbf{\nabla}_x N_I)^{\mathrm{T}}\boldsymbol{\sigma} \otimes (\mathbf{\nabla}_x N_I)\,\mathrm{d}V. \tag{36}$$

On the right-hand side of Eq. (36), the first term is the material stiffness and the second one is the geometric stiffness. In general, during global iteration, the material behavior is linearized according to

$$\Delta\mathbf{S} = \widetilde{\mathscr{K}}\Delta\mathbf{E}, \quad \Delta\boldsymbol{\sigma} = \mathscr{K}\Delta\epsilon \tag{37}$$

with

$$\mathscr{K} = \frac{1}{J}\widetilde{\mathscr{K}} * \mathbf{F}, \tag{38}$$

where $*$ indicates the Rayleigh product which yields

$$\mathscr{K}_{ijkl} = \frac{1}{J}\widetilde{\mathscr{K}}_{mnop}F_{im}F_{jn}F_{ko}F_{lp}. \tag{39}$$

4.2. The local control equations

For each global Newton–Raphson iteration step the deformation gradient $\mathbf{F}$ can be calculated from the approximate displacement field $\hat{\mathbf{u}}$ at every Gauss point. In the local procedure we have to calculate the Cauchy stress $\boldsymbol{\sigma}$ and material stiffness $\mathscr{K}$ on the one hand, and on the other hand the internal variables ρ_{SSD} and ρ_{GND} have to be updated. Therefore, for this nonlocal dislocation model corresponding control functions for these values must be derived first. For the case that the flow and the hardening rules are highly nonlinear, a small time step Δt has to be used during integration, i.e. $\|\mathbf{L}\Delta t\| \ll 1$ and $\|\mathbf{L}_{\mathrm{p}}\Delta t\| \ll 1$. This implies that the exponential function can be approximated by the linear form

$$\mathbf{F}_{\mathrm{p}}^{i+1} = \exp(\mathbf{L}_{\mathrm{p}}\Delta t)\mathbf{F}_{\mathrm{p}}^{i} \cong (\mathbf{I} + \mathbf{L}_{\mathrm{p}}\Delta t)\mathbf{F}_{\mathrm{p}}^{i} \tag{40}$$

and we can use the update equation for $\widetilde{\mathbf{S}}$ as derived by Kalidindi et al. [4]

$$\begin{aligned}\widetilde{\mathbf{S}}_{i+1} \cong \frac{1}{2}\widetilde{\mathscr{K}}_0[(\mathbf{F}_{\mathrm{p}i}^{-\mathrm{T}}\mathbf{C}_{i+1}\mathbf{F}_{\mathrm{p}i}^{-1} - \mathbf{I}) - \sum_{\alpha=0}^{12}(\mathbf{F}_{\mathrm{p}i}^{-\mathrm{T}}\mathbf{C}_{i+1}\mathbf{F}_{\mathrm{p}i}^{-1}\widetilde{\mathbf{M}}^{\alpha}\\ + \widetilde{\mathbf{M}}^{\alpha\mathrm{T}}\mathbf{F}_{\mathrm{p}i}^{-\mathrm{T}}\mathbf{C}_{i+1}\mathbf{F}_{\mathrm{p}i}^{-1})\dot{\gamma}^{\alpha}\Delta t],\end{aligned} \tag{41}$$

$$\mathbf{C}_{i+1} = \mathbf{F}_{i+1}^{\mathrm{T}}\mathbf{F}_{i+1} = 2\mathbf{E}_{i+1} + \mathbf{I}. \tag{42}$$

Finally, we obtain three implicit control equations, namely

$$\widetilde{\mathbf{S}}_{i+1} = \widetilde{\mathbf{S}}_{i+1}(\mathbf{E}_{i+1}, \widetilde{\mathbf{S}}_{i+1}, \rho_{\mathrm{SSD}}^{i+1}, \rho_{\mathrm{GND}}^{i+1}, \Delta t), \tag{43}$$

$$\rho_{\mathrm{SSD}}^{i+1} = \rho_{\mathrm{SSD}}^{i} + \dot{\rho}_{\mathrm{SSD}}^{i+1}(\widetilde{\mathbf{S}}_{i+1}, \rho_{\mathrm{SSD}}^{i+1}, \rho_{\mathrm{GND}}^{i+1}), \Delta t \tag{44}$$

$$\rho_{\mathrm{GND}}^{i+1} = \rho_{\mathrm{GND}}^{i} + \dot{\rho}_{\mathrm{GND}}^{i+1}\left(\mathbf{\nabla}_X \times \left(\dot{\gamma}^{\alpha}\mathbf{F}_{\mathrm{p}}^{\mathrm{T}}\widetilde{\mathbf{n}}^{\alpha}\right), \alpha = 1, N\right)\Delta t. \tag{45}$$

During the simulation we need to calculate the stiffness tensor $\mathscr{K}$ for every Gauss point. According to Eq. (38) we first have to calculate $\widetilde{\mathscr{K}}$. The left part of Eq. (4) yields the tangent stiffness in the reference configuration

$$\widetilde{\mathscr{K}} = \frac{\mathrm{d}\mathbf{S}}{\mathrm{d}\mathbf{E}} = \frac{\partial\mathbf{F}_{\mathrm{p}}^{-1}}{\partial\mathbf{E}}\widetilde{\mathbf{S}}\mathbf{F}_{\mathrm{p}}^{-\mathrm{T}} + \mathbf{F}_{\mathrm{p}}^{-1}\widetilde{\mathbf{S}}\frac{\partial\mathbf{F}_{\mathrm{p}}^{-\mathrm{T}}}{\partial\mathbf{E}} + \mathbf{F}_{\mathrm{p}}^{-1}\frac{\partial\widetilde{\mathbf{S}}}{\partial\mathbf{E}}\mathbf{F}_{\mathrm{p}}^{-\mathrm{T}}. \tag{46}$$

When the control equations (43)–(45) are satisfied, $\frac{\partial\mathbf{F}_{\mathrm{p}}^{-1}}{\partial\mathbf{E}}$, $\frac{\partial\mathbf{F}_{\mathrm{p}}^{-\mathrm{T}}}{\partial\mathbf{E}}$ and $\frac{\partial\mathbf{S}}{\partial\mathbf{E}}$ can be derived. Details are given in Ref. [22,23].

In order to calculate $\dot{\rho}_{\mathrm{GND}}^{i+1}$, the shape functions of the isoparametric element are assumed to also work for $\dot{\gamma}^{\alpha}\mathbf{F}_{\mathrm{p}}^{\mathrm{T}}\widetilde{\mathbf{n}}^{\alpha}$ in Eq. (20). This assumption was earlier also adopted by several other authors [21,22]. We use a trilinear brick element with eight integration points and eight nodes. At first the values of $(\dot{\gamma}^{\alpha}\mathbf{F}_{\mathrm{p}}^{\mathrm{T}}\widetilde{\mathbf{n}}^{\alpha})_I$ at the nodes are calculated from $(\dot{\gamma}^{\alpha}\mathbf{F}_{\mathrm{p}}^{\mathrm{T}}\widetilde{\mathbf{n}}^{\alpha})_{\mathrm{GP}}$ at the Gauss points using the inverse of the shape functions according to

$$(\dot{\gamma}^{\alpha}\mathbf{F}_{\mathrm{p}}^{\mathrm{T}}\widetilde{\mathbf{n}}^{\alpha})_{\mathrm{GP}} = \sum_I N_I(\dot{\gamma}^{\alpha}\mathbf{F}_{\mathrm{p}}^{\mathrm{T}}\widetilde{\mathbf{n}}^{\alpha})_I \Rightarrow (\dot{\gamma}^{\alpha}\mathbf{F}_{\mathrm{p}}^{\mathrm{T}}\widetilde{\mathbf{n}}^{\alpha})_I. \tag{47}$$

This procedure yields eight different values of $\dot{\gamma}^\alpha \mathbf{F}_\mathrm{p}^\mathrm{T} \widetilde{\mathbf{n}}^\alpha$ in each node from the eight adjacent elements[1] and, therefore, the average of these values, $\overline{(\dot{\gamma}^\alpha \mathbf{F}_\mathrm{p}^\mathrm{T} \widetilde{\mathbf{n}}^\alpha)}_I$, is calculated. Finally, the rate of change of the GND density at the integration points can be calculated as

$$\dot{\boldsymbol{\Lambda}}^\alpha = -\frac{1}{b}\widetilde{\mathbf{d}}^\alpha \otimes \sum_I \left[(\boldsymbol{\nabla}_X N_I) \times \overline{(\dot{\gamma}^\alpha \mathbf{F}_\mathrm{p}^\mathrm{T})}_I \widetilde{\mathbf{n}}^\alpha \right]. \tag{48}$$

4.3. The solution algorithms

In general it is not straightforward to formulate a fully implicit Newton–Raphson iteration algorithm for this set of equations. The difficulty arises in particular from Eq. (45) where we need to know the deformation information, **F**, for the neighboring integration points for the calculation of the strain gradient. Owing to this difficulty most nonlocal models use a post-update procedure, when they are built on general-purpose FEM codes, because their material subroutines can only supply the deformation gradient for one integration point, i.e. the deformation information of the neighboring Gauss points can only be obtained from the last converged time step. When using such a post-update nonlocal model one cannot ensure convergence for the GNDs. This means that it is important to develop a robust and generic consistent nonlocal algorithm in order to yield convergence for the GNDs in a FE environment.

4.3.1. The global algorithm

Since the integration points are coupled with each other in the nonlocal model via ρ_GND the update procedures for $\widetilde{\mathbf{S}}_{i+1}$, ρ^{i+1}_SSD, and ρ^{i+1}_GND have to be solved simultaneously. Therefore, we have developed the following solution scheme:

- The iteration identifier, n, in the stress calculation is separated into odd and even valued counts.
- When n is odd, we record the deformation gradient, $\mathbf{F}^n$, for every integration point. Without performing any further calculation we feed an arbitrary constant stress tensor back into the FE algorithm. By doing so we achieve that global convergence cannot be obtained in any odd-valued iteration step. Moreover, we assign a diagonal matrix with very large values to the stiffness tensor, $\mathscr{K}^n$, namely

  $$\mathscr{K}^n_{ijkl} = 0, \quad i \neq k,\ j \neq l,$$
  $$\mathscr{K}^n_{ijkl} = 10^{50}, \quad i = k,\ j = l.$$

- If n is even, due to the form of $\mathscr{K}^n$, the global Newton–Raphson procedure yields

  $$\left(\frac{\partial \mathbf{H}}{\partial \hat{\mathbf{u}}}\right)^{-1}_{n-1} \approx \mathbf{0} \Rightarrow \mathbf{F}^n = \mathbf{F}^{n-1}.$$

  Therefore, the deformation gradient is now known for every integration point, as it was recorded in the previous odd-ordered iteration. With this information the control equations (43)–(45) can be solved using the following local procedure.

4.3.2. The local algorithm

In our approach we use three steps to obtain the final solution for $\widetilde{\mathbf{S}}_{i+1}$, ρ^{i+1}_SSD, and ρ^{i+1}_GND. In the first step we keep ρ^{i+1}_SSD and ρ^{i+1}_GND constant and use the Newton–Raphson algorithm in order to identify $\widetilde{\mathbf{S}}_{i+1}$ and satisfy Eq. (43). In the second step ρ^{i+1}_SSD is calculated using $\widetilde{\mathbf{S}}_{i+1}$. If the difference between the initial value and the newly calculated one is larger than a certain threshold value, steps 1 and 2 are repeated until convergence. When these calculations are finished for all integration points, we proceed to step three, where ρ^{i+1}_GND is calculated using $\widetilde{\mathbf{S}}_{i+1}$ and ρ^{i+1}_SSD as determined in the preceding steps. Again, if the difference between initial and newly calculated values for ρ^{i+1}_GND is larger than a threshold value, steps 1–3 are repeated until convergence is obtained.

5. Application to simple shear of an Al single crystal

The nonlocal dislocation model introduced in this paper is implemented in the commercial FE code MSC.Marc200x in terms of the user defined material subroutine HYPELA2 [25]. The experimental setup and the FE mesh with the eight-noded, isoparametric, three-dimensional brick elements with trilinear interpolation are shown together with the boundary conditions in Fig. 4.

In the FE calculations, the displacements X, Y, and Z of the nodes at the front and back surfaces on the lower part of the mesh were set to zero. This set of boundary conditions is referred to as *apply*1 in Fig. 4. On the upper part of the mesh the displacements Y and Z of the nodes at the front and back surfaces were also set to zero while a constantly increasing value was assigned to the X displacements. This set of boundary conditions is referred to as *apply*2. The orientation data obtained from the microtexture measurements are expressed as $(\varphi_1, \Phi, \varphi_2)$ in Bunge–Euler notation in the RD–TD–ND coordinate system. For the FE analysis the global coordinate system was defined by X parallel to RD, Y parallel to TD and Z parallel to ND. This means that the measured initial orientations were directly assigned to the respective integration points.

The average shear stress–shear strain curve of a simple shear test of an aluminium single crystal with 99.999 wt.% purity (Fig. 5) was used to fit the constitutive parameters of the dislocation model (Table 1). In this process we used the values for the interaction

---

[1] In fact eight adjacent elements apply only for nodes in the volume. For surface nodes the number is smaller.

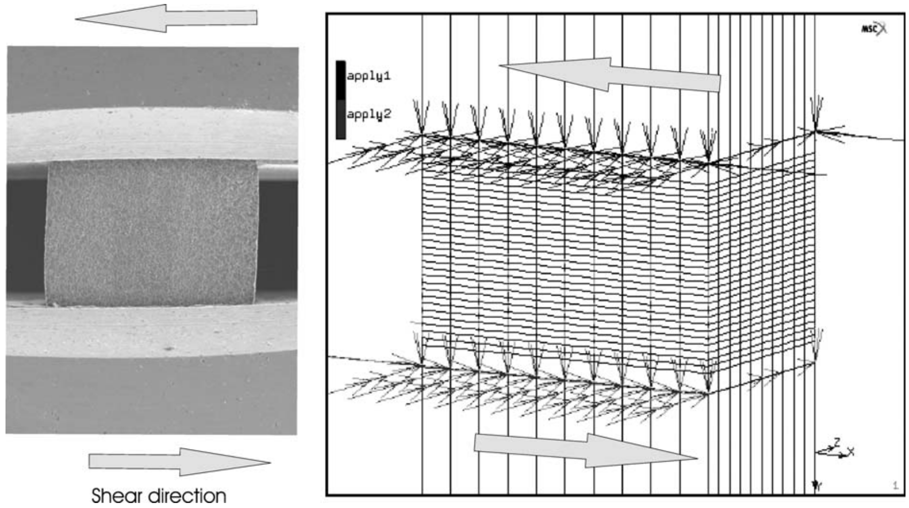

Fig. 4. Experimental setup and the FE mesh used in the simulations indicating also the boundary conditions applied.

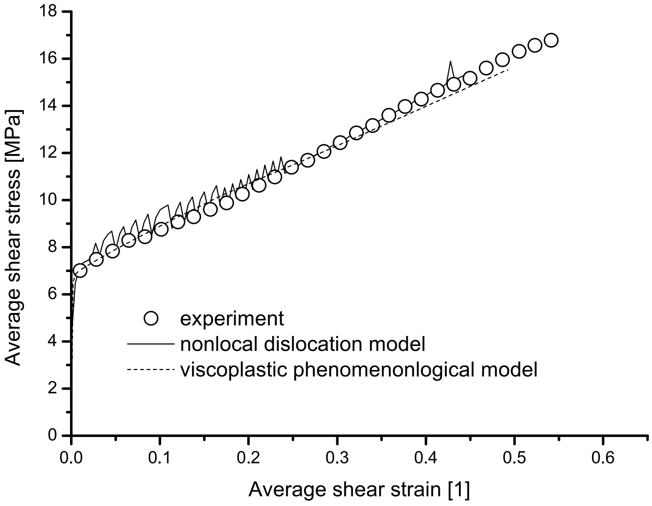

Fig. 5. Parameter determination by a simple shear test of an Al single crystals.

Table 1
The parameters of the nonlocal dislocation model for pure aluminium crystals

Symbol	Value	Meaning
Q_{slip}	3.0×10^{-19} J	Activation energy for slip
Q_{bulk}	2.4×10^{-19} J	Activation energy for climb
c_1	0.1	Constant for passing stress
c_2	2.0	Constant for jump width
c_3	1.0	Constant for obstacle width
c_4	1.5×10^{7} m^{-1}	Constant for lock forming rate
c_5	10.0	Constant for athermal annihilation rate
c_6	1×10^{-30} m^{-1}	Constant for thermal annihilation rate
c_7	1×10^{7} m^5 s^{c_8}	Constant for dipole forming rate
c_8	0.3	Constant for nonlinear climb of edge dislocations

Table 2
The values used for the interaction strength, $\chi^{\alpha\beta}$, as given in Ref. [24]

Interaction/reaction product	$\chi^{\alpha\beta}$
Self-interaction	1.0
Coplanar	2.2
Cross slip	3.0
Glissile junction	3.8
Hirth lock	1.6
Lomer–Cottrell lock	4.5

strength, $\chi^{\alpha\beta}$, as given in Ref. [24] (see Table 2). The initial orientation of the single crystal was $\varphi_1 = 3.4°$, $\Phi = 37.6°$, $\varphi_2 = 36.5°$ and the shear rate amounted to $2.6\times10^{-4}\,\mathrm{s}^{-1}$. During the shear experiments digital images were recorded from the decorated sample surface for photogrammetric analysis providing the von Mises strain distribution for an area of $3.1\times2.2\,\mathrm{mm}^2$. Details of this method were reported in Ref. [26–29]. The simple shear test revealed a rather large inner homogeneous plastic deformation region far away from areas affected by the influence of the boundaries.

The experimental results are compared to simulations achieved using a phenomenological viscoplastic local model [28,29] and the nonlocal model in Fig. 6. In the experiment the maximum deformation occurs in the lower left corner of the single crystal and extends diagonally across the crystal surface. While this behavior is correctly reproduced by the new nonlocal model, the phenomenological viscoplastic model predicts the highest strains in the lower right corner of the specimen. We assume that the better prediction yielded by the new model is mainly a consequence of the introduction of the GNDs and the physically based latent hardening law into the framework. This assumption is supported by the data in Fig. 8(b) which reveal that substantial densities of GNDs are generated near the sample borders. For a better comparison of the relative contributions of the two types of dislocations, Figs. 8(a) and (b) show both the SSD and the GND density distributions on the ND-surface.

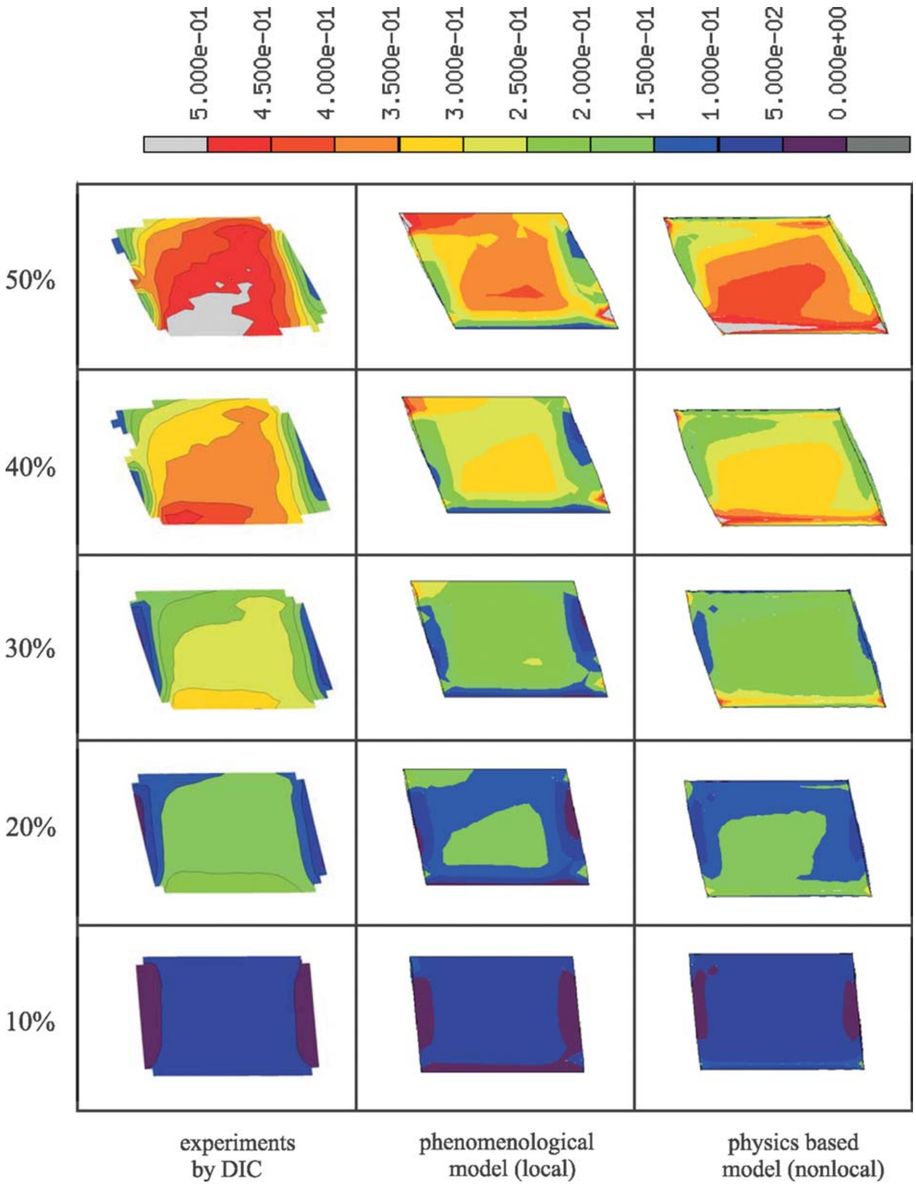

Fig. 6. Comparison of the von Mises strain on the surface of an Al single crystal (3.1 mm long, 2.0 mm thick and 2.2 mm high) for the simple shear test. The first row shows the experimental results obtained by digital image correlation (DIC). The middle row shows the results obtained by using a conventional viscoplastic formulation. The bottom row shows the results obtained by using the new nonlocal formulation as introduced in this work.

5.1. Size dependence of the nonlocal model

The introduction of GNDs renders the new model size sensitive. Therefore, we repeated the shear simulation for a set of three virtual specimens of different height-to-length ratios. For this purpose we changed the height of the sheared sample to one half and one tenth of the original height, respectively. The resulting shear stress–shear strain curves are shown in Fig. 7.

Eqs. (10), (11), (14) and (18) reveal that the GNDs contribute to the passing stress, the cutting stress in the flow rule, and to the multiplication term of the immobile dislocations. For this reason one would expect higher predicted stresses for the thinner samples owing to their relative increase of zones which are mechanically affected by the presence of interfaces. This is indeed confirmed by Fig.7. From Figs. 8(b), (e), (h) it becomes obvious how the relative size of the zone influenced by GNDs increases with decreasing sample height. This increasing GND density entails also an increase of the SSD density as expected and shown in Figs. 8(a), (d), (g). Additionally, Figs. 8(c), (f), (i) also show that the texture evolution of the crystals is changed. This results in an intersection of the stress–strain curves for $H = H_0$ and $H = H_0/2$ in Fig. 7.

The strong influence of the incorporation of the GNDs into the crystal plasticity FE framework on the observed reorientation rates is due to the penalty function they impose. This means that each reorientation step which introduces an orientation divergence with respect to the

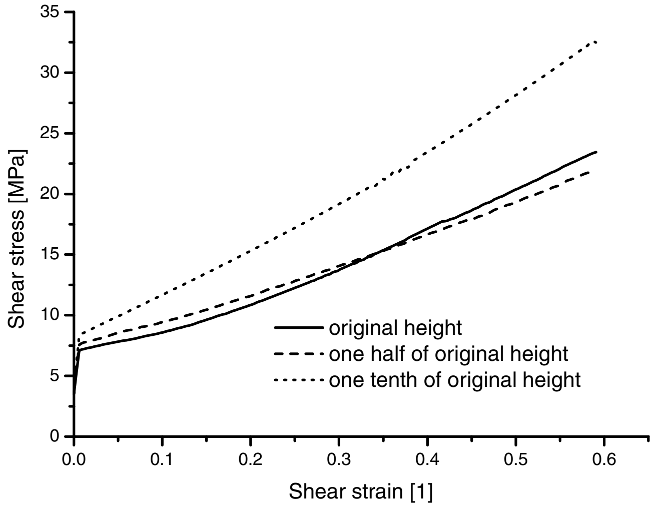

Fig. 7. Simulated shear stress–shear strain curves for samples with different height-to-length ratios demonstrating the size sensitivity of the nonlocal dislocation model.

neighborhood [30] is impeded owing to the corresponding introduction of GNDs.

Fig. 9 shows the profiles of the two immobile dislocation densities (SSDs and GNDs) across the specimen near the sample center for a shear deformation of about 30%. While both dislocation densities are always of the same order of magnitude, their ratio is clearly influenced by the relative sample height. For $H = H_0$ the SSD density is always higher than the GND density. However, this situation is gradually changed with decreasing relative sample height. Finally, for $H = H_0/10$ the GND density surpasses the SSD density near the edges of the heavily sheared zone of the sample.

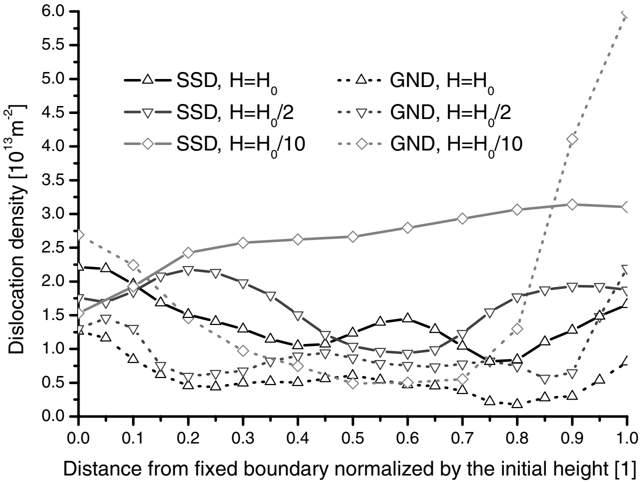

Fig. 9. Comparison of statistically stored and geometrically necessary dislocations for simulated shear tests of samples with different height after 50% shear deformation.

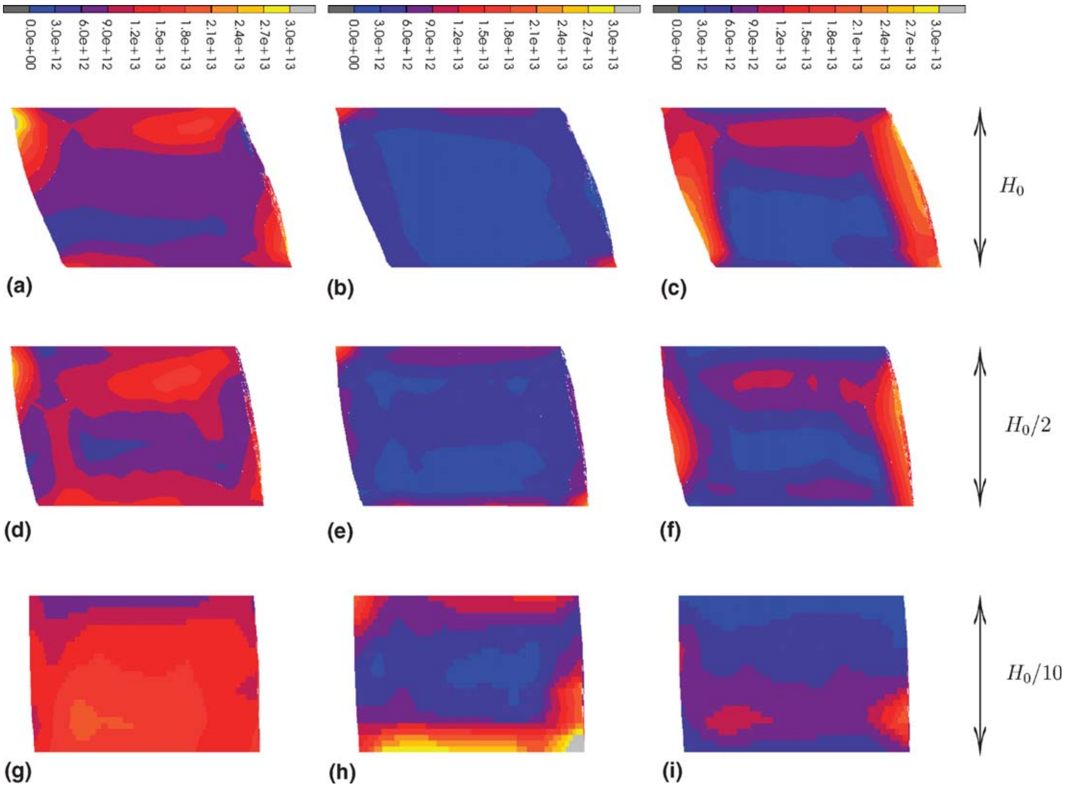

Fig. 8. Comparison of the dislocation densities and misorientation for different samples after 30% shear deformation, (a, b, c), (d, e, f) and (g, h, i) are samples with height $H = H_0$, $H = H_0/2$ and $H = H_0/10$ (all plots are scaled to the same height for better comparison), respectively; (a, d, g), (b, e, h) and (c, f, i) show plots of the statistically stored and geometrically necessary dislocation density and misorientation (orientation change between initial and current orientation), respectively.

6. Conclusions

The mechanical behavior of crystalline matter is a multiscale problem. While the underlying deformation processes such as the slip of dislocations and their reactions and elastic interactions are microscopic problems, the forming process itself is usually of a macroscopic nature. Therefore, the dislocation density based constitutive model developed by Ma and Roters for the fcc crystal structure [11] has been extended to crystal plasticity FE applications. In this context, several modifications and extensions were introduced which allow us to connect the two scales in one common framework. The main modification and extensions are the assumption of a homogeneous dislocation structure which replaces the dislocation cell structure; the introduction of GNDs in addition to the SSDs with the aim to consider strain gradients and thus render the model size sensitive; and the formulation of a consistent algorithm to update the GND density. The latter controls the integration error. The model was implemented into commercial FEM software. A simple shear experiment of an Al single crystal was used for validation. The predicted distribution of the local deformation was found to be in better accordance with the experimental data than for a conventional viscoplastic phenomenological model. We assume that the better prediction yielded by the new model is mainly a consequence of the introduction of the GNDs and the physically based latent hardening law into the framework.

References

[1] Randle V, Engler O. Introduction to texture analysis, macrotexture, microtexture and orientation mapping. Boca Raton (FL): CRC Press; 2000.
[2] Taylor GI. Plastic strain in metals. J Inst Met 1938;62:307–24.
[3] Bronkhorst CA, Kalidindi SR, Anand L. Polycrystalline plasticity and the evolution of crystallographic texture in fcc metals. Philos Trans R Soc A 1992;341(1662):443–77.
[4] Kalidindi SR, Bronkhorst CA, Anand L. Crystallographic texture evolution in bulk deformation processing of fcc metals. J Mech Phys Solids 1992;40:537–69.
[5] Ma A, Roters F, Raabe D. Numerical study of textures and Lankford values for fcc polycrystals by use of a modified Taylor model. Comput Mater Sci 2004;29(3):353–61.
[6] Van Houtte P, Li S, Engler O. Continuum scale simulation of engineering materials. New York: Wiley-VCH; 2004 [chapter: Taylor-type homogenization methods for texture and anisotropy].
[7] Van Houtte P, Li S, Seefeldt M, Delannay L. Deformation texture prediction: from the Taylor model to the advanced lamel model. Int J Plasticity 2005;21(3):589–624.
[8] Ashby MF. The deformation of plastically non-homogenous materials. Philos. Mag. 1970;21:399.
[9] Evers LP, Parks DM, Brekelmans WAM, Geers MGD. Crystal plasticity model with enhanced hardening by geometrically necessary dislocation accumulation. J Mech Phys Solids 2002;50(11):2403–24.
[10] Gao H, Huang Y. Geometrically necessary dislocation and size-dependent plasticity. Scr Mater 2003;48(2):113–8.
[11] Ma A, Roters F. A constitutive model for fcc single crystals based on dislocation densities and its application to uniaxial compression of aluminium single crystals. Acta Mater 2004;52(12):3603–12.
[12] Evers LP, Brekelmans WAM, Geers MGD. Non-local crystal plasticity model with intrinsic ssd and gnd effects. J Mech Phys Solids 2004;52(10):2379–401.
[13] Arsenlis A, Parks DM, Becker R, Bulatov V. On the evolution of crystallographic dislocation density in non-homogeneously deforming crystals. J Mech Phys Solids 2004;52(6):1213–46.
[14] Lee EH. Elastic–plastic deformation at finite strains. Trans ASME E 1969;36(1):1–6.
[15] Peirce D, Asaro RJ, Needleman A. Analysis of nonuniform and localized deformation in ductile single crystals. Acta Metall 1982;30(6):1087–119.
[16] Kocks UF, Argon AS, Ashby AF. Thermodynamics and kinetics of slip. In: Chalmers B, Christian JW, Massalski TB, editors. Progress in materials science, vol. 19. Oxford: Pergamon Press; 1975. p. 1–289.
[17] Nemat-Nasser S, Ni L, Okinaka T. A constitutive model for fcc crystals with application to polycrystalline ofhc copper. Mech Mater 1998;30(4):325–41.
[18] Roters F. A new concept for the calculation of the mobile dislocation density in constitutive models of strain hardening. Phys Stat Sol B 2003;240(1):68–74.
[19] Nye JF. Some geometrical relations in dislocated crystals. Acta Metall 1953;1:153–62.
[20] Dai H, Parks DM. Geometrically-necessary dislocation density and scale-dependent crystal plasticity. In: Khan A, editor. Proceedings of sixth international symposium on plasticity. London: Gordon and Breach; 1997. p. 17–8.
[21] Dai H. Geometrically-necessary dislocation density in continuum plasticty theory, FEM implementation and applications. PhD thesis, Massachusetts Institute of Technology; 1997.
[22] Meissonnier FT, Busso EP, O'Dowd NP. Finite element implementation of a generalised non-local rate-dependent crystallographic formulation for finite strains. Int J Plasticity 2001;17(4):601–40.
[23] Ma A. Implicit scheme of rve calculation for fcc polycrystals. Comput Mater Sci 2003;27(4):471–9.
[24] Arsenlis A, Parks DM. Modeling the evolution of crystallographic dislocation density in crystal plasticity. J Mech Phys Solids 2002;50(9):1979–2009.
[25] MSC.Marc user's manual 2003. User subroutines and special routines, Volume D; 2003.
[26] Sachtleber M, Zhao Z, Raabe D. Experimental investigation of plastic grain interaction. Mater Sci Eng A 2002;336(1–2): 81–7.
[27] Zaefferer S, Kuo J-C, Zhao Z, Winning M, Raabe D. On the influence of the grain boundary misorientation on the plastic deformation of aluminum bicrystals. Acta Mater 2003;51(16):4719–35.
[28] Roters F, Wang Y, Kuo J-C, Raabe D. Comparison of single crystal simple shear deformation experiments with crystal plasticity finite element simulations. Adv Eng Mater 2004;6(8):653–6.
[29] Kuo J-C. Mikrostrukturmechanik von Bikristallen mit Kippkorngrenzen. PhD thesis, RWTH Aachen; 2004.
[30] Raabe D, Zhao Z, Park SJ, Roters F. Theory of orientation gradients in plastically strained crystals. Acta Mater 2002;50:421–40.